ChemComm

Check for updates

A class of metal diboride electrocatalysts synthesized by a molten salt-assisted reaction for the hydrogen evolution reaction†

Feifan Guo,‡[a] Yuanyuan Wu,‡[ab] Xuan Ai, [iD] ‡[a] Hui Chen,[a] Guo-Dong Li, [iD] [a] Wei Chen[c] and Xiaoxin Zou [iD] *[a]
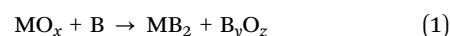
A family of twelve monometallic diborides, containing transition metals from group IVB elements to group VIII elements, and Ni–W bimetallic diborides are synthesized *via* a molten salt-assisted method. Their trend in activity for the hydrogen evolution reaction is studied, with Ni–W bimetallic diborides acting as the most efficient, nonprecious electrocatalysts.

Metal borides (also known as metal–boron intermetallic compounds) are a class of boron-bearing alloy materials with ordered crystal structure and defined stoichiometry. Metal borides have high chemical, thermal, and mechanical stability in general because of their distinctive, complex metal–metal, metal–boron and boron–boron bonding features.[1] Some metal borides have been discovered to possess impressive physical properties for over ten years, such as superconductivity and superhardness.[2,3] However, not until recent years have the remarkable catalytic properties of borides come into focus for research.[4–6] The relatively sluggish study of borides' catalytic functions is partially due to a lack of appropriate boride samples that can be employed for catalysis investigation. First, the majority of boride samples with well-defined structures, including those that have been used for the study of physical properties, are prepared under extreme conditions, *e.g.*, high temperature and high pressure.[4,7] Such boride samples are generally composed of bulk particles in a small quantity, and thus, are difficult to branch out to catalysis study. Second, although there are a few methods to synthesize metal borides under mild conditions, the resulting samples are often limited in elemental composition and crystal structure.[6]

Third, metal borides often have many phase variations with tiny stoichiometric differences, and thereby the synthesis of phase-pure target products is difficult.[8] Therefore, developing general routes toward the synthesis of phase-pure borides under relatively mild conditions is crucial for the discovery of efficient boride catalysts.

On the other hand, in comparison with some well-studied materials (*e.g.*, MoS_2), metal diborides (*e.g.*, $\alpha\text{-}MoB_2$) recently emerged as promising electrocatalysts for the hydrogen evolution reaction (HER) due to their better electronic conductivity and higher density of active sites.[4] In this regard, $\alpha\text{-}MoB_2$ as the first and prominent diboride catalyst has been reported by our group and Fokwa's group separately to show better electrocatalytic activity for HER than other crystal phases of molybdenum borides, such as MoB and Mo_2B.[4,9] The presence of borophene subunits (or graphene-like boron sheet motifs) has been demonstrated to be the key to the high electronic conductivity and large density of the active sites of $\alpha\text{-}MoB_2$. Inspired by these successes, the other objective in this work is to provide some fundamental understanding of the trend in activity on a family of metal diborides and to find a novel diboride-based catalytic material with higher catalytic activity.

Herein, we present a general molten salt-assisted route[10] to synthesize a class of twelve monometallic diborides and then investigate their trend in electrocatalytic activity for HER. Among them, ruthenium diboride is the highest active catalyst, and tungsten diboride is the best nonprecious catalyst for HER. Furthermore, the doping of nickel in tungsten diboride is shown to optimize the electronic structure of the latter, thereby significantly improving the electrocatalytic activity.

$$MO_x + B \rightarrow MB_2 + B_yO_z \qquad (1)$$

We synthesize twelve monometallic diborides by a boron thermal reaction under a KCl–NaCl molten salt condition (eqn (1), M represents transition metal), followed by the removal of the byproduct (*i.e.*, boron oxides) with hot water[11] (see Experimental details in ESI,† Fig. S1 and Table S1). The synthesis of metal diborides generally employs the corresponding metal

[a] State Key Laboratory of Inorganic Synthesis and Preparative Chemistry, College of Chemistry, Jilin University, Changchun 130012, P. R. China. E-mail: xxzou@jlu.edu.cn

[b] Key Laboratory of Preparation and Application of Environmental Friendly Materials (Jilin Normal University), Ministry of Education, Changchun 130103, P. R. China

[c] Laboratory of Theoretical and Computational Chemistry, Institute of Theoretical Chemistry, Jilin University, Changchun 130023, P. R. China

† Electronic supplementary information (ESI) available. See DOI: 10.1039/c9cc03638e

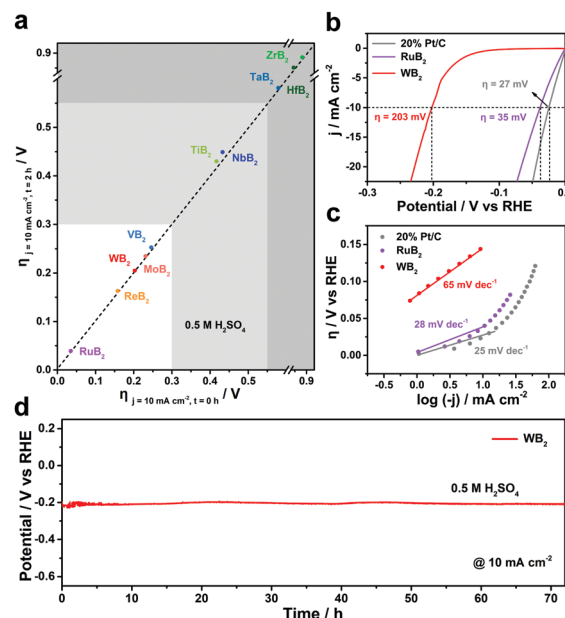‡ F. Guo, Y. Wu and X. Ai contributed equally to this work.
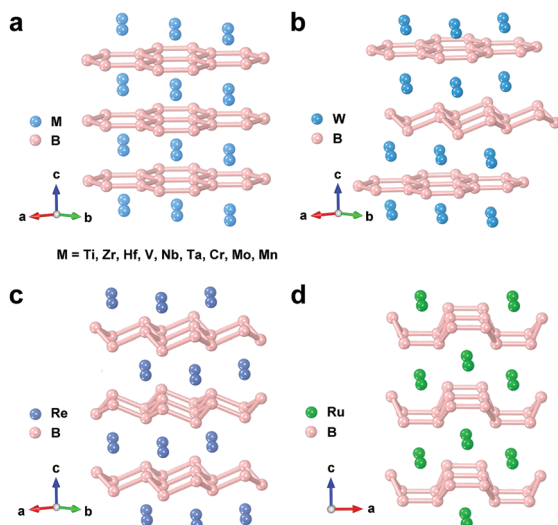
Fig. 1 The crystal structures of twelve metal diborides: (a) MB_2 (M = Ti, Zr, Hf, V, Nb, Ta, Cr, Mo, and Mn), (b) WB_2, (c) ReB_2, and (d) RuB_2. The pink balls represent boron atoms, whereas the light blue, blue, bluish violet and green balls represent the corresponding metal atoms.

Fig. 2 (a) The catalytic activity and short-term stability of metal diborides for the HER. The x-axis and y-axis are the overpotentials required to achieve 10 mA cm^{-2} per geometric area at time t = 0 h and t = 2 h. The dashed line represents the ideal stable catalyst response. (b) Polarization curves of WB_2, RuB_2 and 20% Pt/C for the HER in 0.5 M H_2SO_4 solution with 85% iR-compensation. (c) Tafel plots of WB_2, RuB_2 and 20% Pt/C for the HER. (d) $V-t$ curve of WB_2 in 0.5 M H_2SO_4 solution at 10 mA cm^{-2}.

oxides as the starting material, except the synthesis of ReB_2 with metallic Re as the precursor.

The resulting twelve monometallic diborides include TiB_2, VB_2, CrB_2, MnB_2, ZrB_2, NbB_2, MoB_2, HfB_2, TaB_2, WB_2, ReB_2 and RuB_2. As shown in Fig. 1, the twelve metal diborides adopt four types of crystal structures. Their conspicuous structural difference lies in the different two-dimensional covalent boron sheet subunits. The boron sheet subunit in MB_2 is graphene-like, where M = Ti, Zr, Hf, V, Nb, Ta, Cr, Mo or Mn. While WB_2 contains both graphene-like and puckered-type boron sheet subunits, ReB_2 and RuB_2 comprise puckered boron motifs in "chair" and "boat" conformations, respectively.

The powder X-ray diffraction (XRD) patterns in Fig. S2 (ESI†) confirm the synthesis of pure MB_2 phases. Transmission electron microscopy images (TEM, Fig. S3, ESI†) present that TiB_2, ZrB_2, HfB_2, VB_2, CrB_2 and ReB_2 possess a nanosheet structure, NbB_2, TaB_2 and MnB_2 have a needle structure, and MoB_2, WB_2 and RuB_2 consist of aggregated nanoparticles. The Brunauer–Emmett–Teller (BET) specific surface areas for these MB_2 are in the range of 5–30 m^2 g^{-1}, except for ZrB_2 and HfB_2 (about 70 m^2 g^{-1}, Table S2, ESI†). These results suggest that the molten salt-assisted method provides a route for the controllable synthesis of metal diborides.

We study the electrocatalytic activity of the as-obtained metal diborides toward HER in acidic solution. Note that CrB_2 and MnB_2 are not further investigated because they are soluble in acidic solution. Fig. S4 (ESI†) shows the polarization curves for the HER over MB_2 (M = Ti, Zr, Hf, V, Nb, Ta, Cr, Mo, and Mn). Their overpotentials required to reach the current density of 10 mA cm^{-2} (the approximate current density expected for an integrated solar water-splitting device under 1 sun illumination operating at 10% solar-to-fuels efficiency) are listed in Fig. 2a to evaluate activity.[12] These MB_2 can be divided into three groups in activity: (i) ZrB_2, HfB_2 and TaB_2 (dark grey region) have an overpotential greater than 550 mV at 10 mA cm^{-1}, indicating

their poor catalytic performances; (ii) TiB_2 and NbB_2 (light gray region) have moderate catalytic properties; and (iii) RuB_2, ReB_2, WB_2, MoB_2 and VB_2 (white region) have desirable properties, where the overpotentials required to achieve 10 mA cm^{-2} are less than 300 mV. Moreover, these MB_2 catalysts have almost no loss of activity after 2 h of constant polarization, suggesting that they have good stability in catalysing HER.

Among them, the RuB_2 shows the highest catalytic activity, achieving 10 mA cm^{-2} at an overpotential of 35 mV, close to that of 20% Pt/C in acidic solution (Fig. 2b). And the WB_2 exhibits the best activity among non-precious metal diborides, obtaining 10 mA cm^{-2} at an overpotential of 203 mV. Their activity trends are further supported by comparing the Tafel slopes in Fig. 2c, which shows that RuB_2 has a Tafel slope of 28 mV dec^{-1}, close to that of 20% Pt/C (25 mV dec^{-1}) and WB_2 has a Tafel slope of 65 mV dec^{-1}. These results indicate that hydrogen evolution over RuB_2 and WB_2 should occur via the Volmer–Tafel mechanism and Volmer–Heyrovsky mechanism, respectively. The rate-determining step for the former is the recombination step of two adsorbed H atoms (H_{ads} + H_{ads} → H_2), and for the latter it is an electrochemical desorption step (H_{ads} + H_3O^+ + e^- → H_2 + H_2O). Further catalytic measures are performed to present WB_2 as a promising non-precious catalyst for HER. As shown in Fig. 2d, WB_2 retains its electro-catalytic activity at 10 mA cm^{-2} for 70 h, suggesting its long-time stability during HER. Additionally, WB_2 exhibits a nearly 100% faradaic efficiency (Fig. S5, ESI†), suggesting that the total charge passed through the catalyst is used for HER.

In order to further improve the catalytic activity of WB$_2$, heteroatom incorporation is considered to be an effective strategy by modulating the electronic structure. We synthesized Ni-doped WB$_2$ (Ni–WB$_2$, see Experimental details in ESI†) and then investigated its activity for catalyzing HER. A series of $x\%$ Ni–WB$_2$ catalysts were synthesised ($x\%$ represents molar percentage of Ni, metal base). 10% Ni–WB$_2$ presents the optimal catalytic activity (Fig. S6, ESI†), and hence most of the characterizations focus on this particular sample. The X-ray photoelectron spectroscopy (XPS) spectrum and Energy Dispersive spectrum (EDS) of 10% Ni–WB$_2$ verify the existence of Ni in the structure of WB$_2$ (Fig. S7 and S8, ESI†). The X-ray diffraction (XRD) patterns (Fig. S7a, ESI†) present that the Ni atom doping does not change the crystal structure of WB$_2$. The diffraction peaks of 10% Ni–WB$_2$ shift slightly to higher angles, compared with the undoped WB$_2$. This indicates that Ni atoms have successfully substituted W atoms in the WB$_2$ lattice and decrease the lattice distance because the radius of Ni is smaller than W.[13] The transmission electron microscopy (TEM) images (Fig. S9a, ESI†) show that the 10% Ni–WB$_2$ maintains the nanoparticle morphology (50–200 nm in size). Elemental mapping images (Fig. 3a) show that the uniform distribution of Ni, W and B elements over the entire particles. In the high-resolution transmission electron microscopy (HRTEM) image (Fig. S9b, ESI†) of 10% Ni–WB$_2$, the lattice spacing of 0.254 nm can be indexed to the (101) plane of the WB$_2$ phase, respectively.

Next, we investigated the effect of Ni doping on the catalytic performance of WB$_2$ for HER in 0.5 M H$_2$SO$_4$. Fig. 3b shows the polarization curves for the HER over pure WB$_2$ and 10% Ni–WB$_2$. As observed, Ni doping significantly increases the catalytic activity

in the acid of WB$_2$. In particular, the electrocatalytic activity of Ni doped WB$_2$ is about 8.4 times higher than WB$_2$ in acidic conditions, with the current densities 11.2 and 1.33 mA cm^{-1}, respectively, at 0.15 V *vs.* RHE. In addition, the Ni-doped WB$_2$ also has a better HER performance than WB$_2$ in basic solution (Fig. S10, ESI†). Fig. 3c shows that 10% Ni–WB$_2$ has a similar Tafel slope with WB$_2$, indicating that Ni doping does not change the reaction path for hydrogen evolution. Meanwhile, 10% Ni–WB$_2$ maintains a good stability and nearly 100% faradaic yield during HER (Fig. 3d and e). After 15 h stability test, its surface components and morphology also remain unchanged (Fig. S11, ESI†).

In order to examine the role of surface structure in influencing the catalytic activity, we assessed the surface areas for pure WB$_2$ and 10% Ni–WB$_2$ by BET surface areas (Table S2, ESI†) and electrochemical active surface areas (ECSA, Fig. S12, ESI†). The results reveal that the two materials have similar surface areas obtained from either method. This indicates that the significantly enhanced activity of 10% Ni–WB$_2$ is not originated from increasing the surface area or the number of active sites. That is, the Ni doping improves the intrinsic HER activity of WB$_2$. This result can further be supported by the electrochemical impedance spectroscopy, which shows that the electron transfer rates and reaction kinetics during HER is much faster after Ni doping (Fig. S13, ESI†).

Density functional theory calculations (DFT) were performed to uncover how Ni doping synergistically enhances the catalytic activity of WB$_2$ toward HER. The hydrogen adsorption free energy (ΔG_{H^*}) is widely used as a theoretical activity descriptor, determining the overall reaction kinetics of the HER on catalyst surfaces.[14] The optimum catalysts should have a near-zero ΔG_{H^*} value. We calculated ΔG_{H^*} values for stable H* adsorption sites on two B-terminated (001) surfaces and two W-terminated (001) surfaces for pure WB$_2$ and Ni–WB$_2$, respectively (Fig. 4a, b and Fig. S15, S16, ESI†). The results (Tables S3–S6, ESI†) suggest that the B1-terminated (001) surface and W1-terminated (001) surface constitute more efficient catalytic sites with respect to the B2-terminated (001) surface and W2-terminated (001) surface. Hence, we further compare the catalytic activities for HER on the
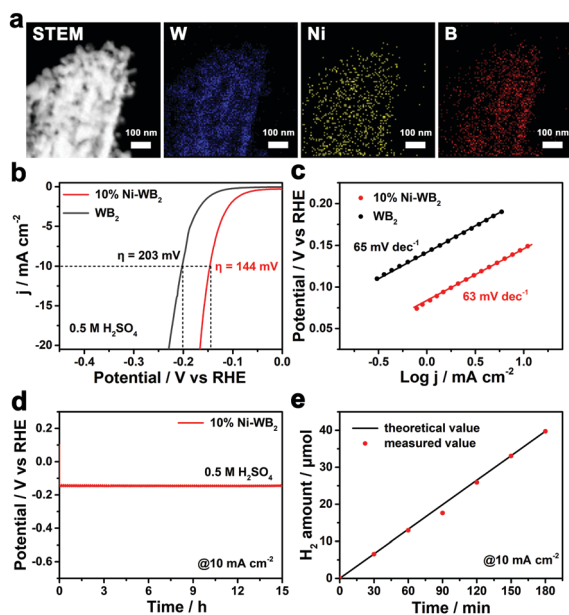

Fig. 3 (a) STEM image and corresponding EDX mapping images of 10% Ni–WB$_2$. (b) Polarization curves of 10% Ni–WB$_2$ and WB$_2$ for the HER in 0.5 M H$_2$SO$_4$ solution with 85% iR-compensation. (c) Tafel plots of 10% Ni–WB$_2$ and WB$_2$ for the HER. (d) V–t curve of 10% Ni–WB$_2$ in 0.5 M H$_2$SO$_4$ solution at 10 mA cm^{-2}. (e) The faradaic efficiency of 10% Ni–WB$_2$.
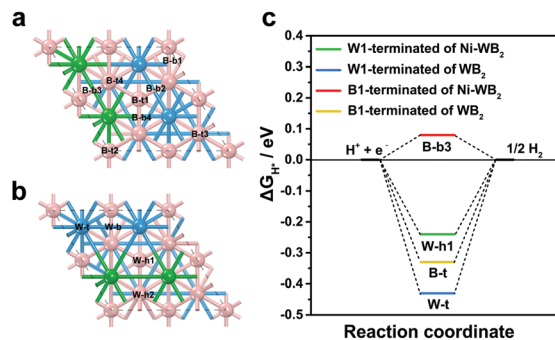

Fig. 4 Stable H* adsorption sites on the (a) graphene-like B1 terminated (001) surface and (b) metal W1 terminated (001) surfaces of Ni–WB$_2$. (c) The calculated free-energy diagram of the HER at equilibrium potential for the most active adsorption sites of H* on the (001) surface of WB$_2$ and Ni–WB$_2$.

B1-terminated (001) surfaces and W1-terminated (001) surfaces of WB_2 and $Ni-WB_2$ (Tables S7–S9, ESI†). Fig. 4a and b show that the stable H adsorption sites of $Ni-WB_2$ on the B1-terminated (001) surfaces include four B top sites (*i.e.*, B-t1, t2, t3, and t4) and four bridge sites (*i.e.*, B-b1, b2, b3, and b4), and that W1-terminated (001) surfaces include one W top site (*i.e.*, W-t), one bridge site (*i.e.*, W-b) and two hollow sites (*i.e.*, W-h1, h2). The ΔG_{H^*} values of the most catalytically active sites on the two surfaces (*i.e.*, B-b3 and W-h1) of $Ni-WB_2$ are listed in Fig. 4c. For comparative purposes, the ΔG_{H^*} values of the catalytically active sites (*i.e.*, B-t and W-t) of WB_2 are included. Compared with WB_2, both the W1-terminated (001) surface and B1-terminated (001) surface of $Ni-WB_2$ have a higher catalytic activity for HER, as reflected by their smaller ΔG_{H^*} absolute values.

The decreased ΔG_{H^*} after Ni doping should be attributed to the modification of electronic structure. For the W1-terminated (001) surface, the d-band center of $Ni-WB_2$ shifts from -1.55 eV to -1.69 eV compared with that of WB_2 (Fig. S17, ESI†). This means more occupied antibonding states on the W1-terminated (001) surface of $Ni-WB_2$, resulting in weaker H adsorption. In addition, for the B1-terminated (001) surface, the Bader charge analysis shows that Ni doping decreases the negative charge of the surface boron atoms (-0.30 $|e|$ for WB_2 and -0.22 $|e|$ for $Ni-WB_2$), decreasing the B–H bond strength (Table S10, ESI†). These results confirm that both the B-terminated (001) surface and W-terminated (001) surface of $Ni-WB_2$ show an optimized electronic structure, thereby significantly improving the catalytic activity for HER.

In summary, we have provided a molten salt-assisted method to synthesize a family of twelve monometallic diborides and investigated their activity trend toward the HER. We also propose a Ni doping strategy to enhance the intrinsic catalytic activity of WB_2 by engineering its electronic structure at the catalytic surfaces.

Conflicts of interest

There are no conflicts to declare.

Notes and references

1. (a) S. Carenco, D. Portehault, C. Boissière, N. Mézailles and C. Sanchez, *Chem. Rev.*, 2013, **113**, 7981–8065; (b) G. Akopov, M. T. Yeung and R. B. Kaner, *Adv. Mater.*, 2017, **29**, 1604506; (c) G. Gouget, P. Beaunier, D. Portehault and C. Sanchez, *Faraday Discuss.*, 2016, **191**, 511–525.
2. J. Nagamatsu, N. Nakagawa, T. Muranaka, Y. Zenitani and J. Akimitsu, *Nature*, 2001, **410**, 63–64.
3. R. B. Kaner, J. J. Gilman and S. H. Tolbert, *Science*, 2005, **308**, 1268–1269.
4. (a) Y. Chen, G. Yu, W. Chen, Y. Liu, G. D. Li, P. Zhu, Q. Tao, Q. Li, J. Liu, X. Shen, H. Li, X. Huang, D. Wang, T. Asefa and X. Zou, *J. Am. Chem. Soc.*, 2017, **139**, 12370–12373; (b) H. Park, Y. Zhang, J. P. Scheifers, P. R. Jothi, A. Encinas and B. P. T. Fokwa, *J. Am. Chem. Soc.*, 2017, **139**, 12915–12918.
5. (a) F. Guo, Y. Wu, H. Chen, Y. Liu, L. Yang, X. Ai and X. Zou, *Energy Environ. Sci.*, 2019, **12**, 684–692; (b) J. Li, H. Chen, Y. Liu, R. Gao and X. Zou, *J. Mater. Chem. A*, 2019, **7**, 5288–5294; (c) H. Li, H. Wen, Q. Li, C. Dun, J. Xing, C. Lu, S. Adhikari, L. Jiang, D. L. Carroll and S. M. Geyer, *Adv. Energy Mater.*, 2017, **7**, 1700513.
6. (a) Q. Li, X. Zou, X. Ai, H. Chen, L. Sun and X. Zou, *Adv. Energy Mater.*, 2019, **9**, 1803369; (b) D. Portehault, S. Devi, P. Beaunier, C. Gervais, C. Giordano, C. Sanchez and M. Antonietti, *Angew. Chem., Int. Ed.*, 2011, **50**, 3262–3265.
7. Q. Tao, D. Zheng, X. Zhao, Y. Chen, Q. Li, Q. Li, C. Wang, T. Cui, Y. Ma, X. Wang and P. Zhu, *Chem. Mater.*, 2014, **26**, 5297–5302.
8. (a) W. J. Jiang, S. Niu, T. Tang, Q. H. Zhang, X. Z. Liu, Y. Zhang, Y. Y. Chen, J. H. Li, L. Gu, L. J. Wan and J. S. Hu, *Angew. Chem., Int. Ed.*, 2017, **56**, 6572–6577; (b) J. Jiang, M. Wang, W. Yan, X. Liu, J. Liu, J. Yang and L. Sun, *Nano Energy*, 2017, **38**, 175–184.
9. H. Park, A. Encinas, J. P. Scheifers, Y. Zhang and B. P. T. Fokwa, *Angew. Chem., Int. Ed.*, 2017, **56**, 5575–5578.
10. (a) X. Liu, N. Fechler and M. Antonietti, *Chem. Soc. Rev.*, 2013, **42**, 8237–8265; (b) J. Zhou, J. Lin, X. Huang, Y. Zhou, Y. Chen, J. Xia, H. Wang, Y. Xie, H. Yu, J. Lei, D. Wu, F. Liu, Q. Fu, Q. Zeng, C. H. Hsu, C. Yang, L. Lu, T. Yu, Z. Shen, H. Lin, B. I. Yakobson, Q. Liu, K. Suenaga, G. Liu and Z. Liu, *Nature*, 2018, **556**, 355–359.
11. S. Ran, H. Sun, Y. Wei, D. Wang, N. Zhou and Q. Huang, *J. Am. Ceram. Soc.*, 2014, **97**, 3384–3387.
12. (a) C. C. L. McCrory, S. Jung, I. M. Ferrer, S. M. Chatman, J. C. Peters and T. F. Jaramillo, *J. Am. Chem. Soc.*, 2015, **137**, 4347–4357; (b) Y. Gorlin and T. F. Jaramillo, *J. Am. Chem. Soc.*, 2010, **132**, 13612–13614; (c) M. G. Walter, E. L. Warren, J. R. McKone, S. W. Boettcher, Q. Mi, E. A. Santori and N. S. Lewis, *Chem. Rev.*, 2010, **110**, 6446–6473.
13. (a) E. Clementi, D. L. Raimondi and W. P. Reinhardt, *J. Chem. Phys.*, 1967, **47**, 1300; (b) S. T. Renosto, R. Lang, E. Diez, L. E. Corrêa, M. S. da Luz, Z. Fisk and A. J. S. Machado, *J. Alloys Compd.*, 2019, **787**, 414–422.
14. B. Hinnemann, P. G. Moses, J. Bonde, K. P. Jørgensen, J. H. Nielsen, S. Horch, I. Chorkendorff and J. K. Nørskov, *J. Am. Chem. Soc.*, 2005, **127**, 5308–5309.